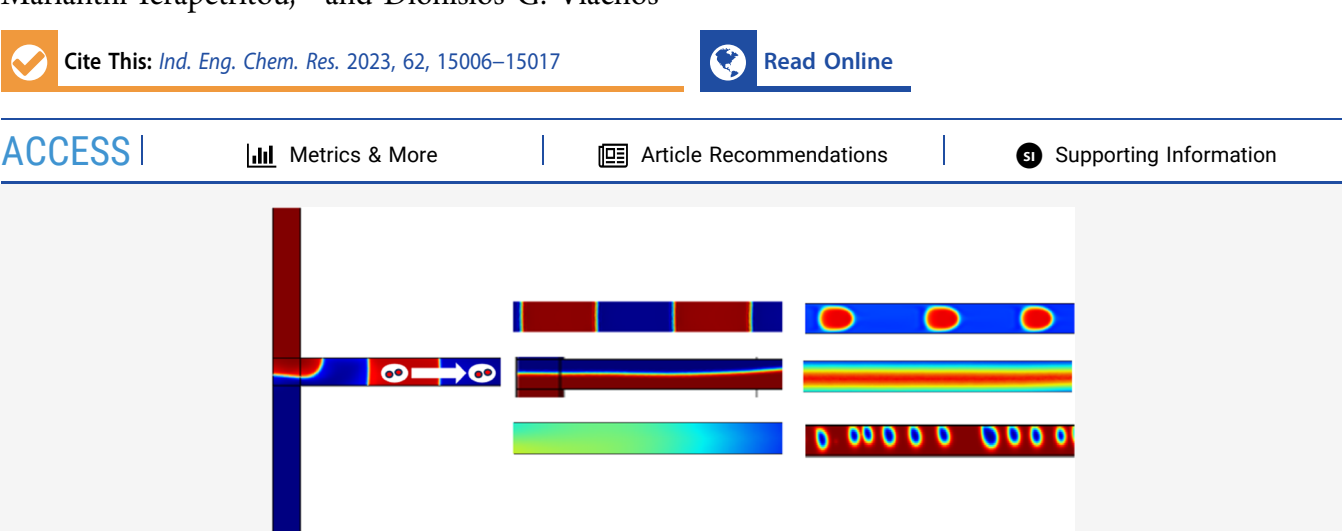


pubs.acs.org/IECR Article

Effect of Scale-Up on Mass Transfer and Flow Patterns in Liquid-Liquid Flows Using Experiments and Computations

Published as part of the Industrial & Engineering Chemistry Research virtual special issue "Dmitry Murzin Festschrift".

Arnav Mittal, Souryadeep Bhattacharyya, Matthew Marino, Tai-Ying Chen, Pierre Desir, Marianthi Ierapetritou,* and Dionisios G. Vlachos*



ABSTRACT: Liquid—liquid microchannels have high mass transfer rates but low throughput. To increase productivity, they can be scaled up by increasing the diameter. Therefore, predicting flow patterns and mass transfer rates while accounting for solvent effects as the diameter varies is crucial; however, this topic is currently lacking in the literature. We develop random forest and symbolic genetic regression machine learning (ML) models to predict flow patterns and the mass transfer rate, respectively, using a combination of our experimental and computational fluid dynamics (CFD) data and literature-mined data, while accounting for the effects of solvent properties and channel diameter. This enables rapid prediction for efficient scale-up of microchannels to millichannels. To minimize the number of CFD simulations and maximize the model accuracy, we employ active learning techniques. Furthermore, we quantify the uncertainty of the ML models built on the hybrid data.

■ INTRODUCTION

Recent developments in microfluidic technology have enabled process intensification and miniaturization of chemical processes. Microstructured devices usually consist of channels with diameters of less than 1 mm.^{1–3} Their small characteristic length scale enables large surface-to-volume ratios. As a result, the heat and mass transfer rates surpass those of traditional large-scale batch or continuous flow reactors.^{4–11} Fast mass transfer and laminar flow allow for precise control over residence time.^{4,12–15} These characteristics lead to significant advantages in nitration, polymerization, and rearrangement reactions.^{5,16–22}

Liquid—liquid biphasic microchannels exhibit various flow patterns that impact transport rates. ^{23–25} These can be engineered by changing solvents (density, viscosity, and surface tension), the fraction of each phase, the micromixer where the streams intersect (T-junction, Y-junction, etc.), the wall hydrophilicity, and the channel diameter, length, and geometry. ^{26–31} This tunability can significantly improve the reactor throughput. The most common patterns are segmented

(slugs and droplets) and parallel flow. In the former, the two liquids form alternating segments where the wall-wetting fluid (continuous phase) usually forms a thin film around the nonwetting fluid (dispersed phase).^{32,33} In the latter, one fluid flows alongside the other.^{4,34} Parallel flow has found application in liquid—liquid extraction and characterization of various products, such as metals, metal complexes, and DNA,^{35–37} achieving high extraction efficiency within reduced contact times.³⁸ Segmented flow, on the other hand, keeps the dispersed phase away from the wall, and the strong inner recirculation enhances mass transfer, producing well-controlled nanoparticles.^{4,13,39,40} Segmented flows have also been used in

Received: July 5, 2023
Revised: August 26, 2023
Accepted: August 28, 2023
Published: September 6, 2023





the conversion of lignocellulosic biomass, such as the conversion of glucose and fructose to 5-hydroxymethylfurfural (HMF). 4,7,41,42

While microchannels offer advantages, they possess a low throughput and a relatively higher-pressure drop. Scaling out to a suitable throughput requires many channels, resulting in more wall material for construction. In recent work, we proposed scaling-up the basic unit, until performance starts decreasing, followed by numbering up (several channels placed in parallel).^{7,43} Determining the "critical size" above which the microscale advantages diminish is important.⁴⁴

Traditionally, dimensionless numbers, such as the Ca (Capillary number), Re (Reynolds number), We (Weber number), and Oh (Ohnesorge number), of both phases are used to predict flow patterns. However, these flow maps do not hold as solvents, and the diameter change. Desir et al. used a decision tree model to predict flow patterns for multiple solvents using six features and achieved $\geq 95\%$ accuracy. Wang et al. investigated liquid—liquid mass transfer for multiple diameters and lengths and proposed a correlation for the mass transfer rate in the mm scale. Chen et al. studied the HMF liquid—liquid extraction for multiple solvents experimentally and computationally. Other studies have also tried to predict the impact of diameter or length, but solvent effects and uncertainty quantification associated with the data have been lacking. 9.12,27,45-50

We aim to predict the impact of the diameter and solvent on flow patterns and mass transfer rates. To achieve this, we conducted experiments and computational fluid dynamics (CFD) simulations to account for the effects of solvent and diameter. To reduce the number of CFD simulations, we employ an active learning algorithm.⁵¹ We complement our data with mined literature experimental data and integrate these data sets, considering their uncertainties and fidelity.⁵ We propose a ML model to predict the flow patterns and introduce a new functional form of mass transfer involving dimensionless numbers utilizing symbolic genetic regression. Our work provides a prediction tool for selecting parameters, such as velocity, diameter, and length, to achieve a certain flow pattern and mass transfer coefficient. Additionally, the results provide insights into scale-up and solvent selection for the enhanced mass transfer rate.

The structure of this article is as follows. We introduce the experimental and computational methodology to investigate liquid—liquid flow patterns and mass transfer rates, followed by the need to use a hybrid data set and account for uncertainties. The Results and Discussion section details the simulation and experimental data for flow patterns followed by the mass transfer rate topic. Finally, the Conclusions summarize our main findings and suggest directions for future research.

SYSTEMS AND METHODS

T-Junction Microchannel. In this study, we utilize horizontally placed T-junction microchannel^{12,26} where an organic phase and an aqueous phase mix, as shown in Figure 1. A T-junction was selected for this study, as it enhances mass transfer due to increased interfacial area created at the junction when the liquids come in contact. T-junctions can be easily scaled-up in industrial processes. The interplay of viscous, interfacial, inertial, and gravitational forces creates multiple flow patterns^{4,6,19} identified based on standard definitions; see SI. ^{4,28,34,46,53} For the mass transfer rate study, an aqueous phase consisting of HMF and an organic phase free of HMF

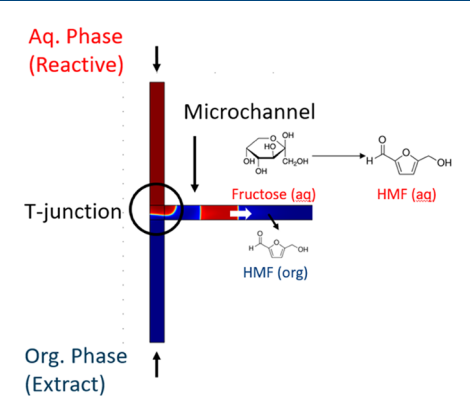


Figure 1. T-junction microchannel geometry built in COMSOL with an aqueous and an organic phase inlet each.

are sent to the T junction, and HMF is transferred from the aqueous phase to the organic phase.

Experimental Methods. Two syringe pumps (ReaXus LS Class High Performance Isocratic pumps) were used to pump the aqueous and organic solvent feed into a square crosssection T-junction (Valco Instruments) made of poly(ether ketone) (PEEK), as seen in Figure S1. The biphasic mixture then enters a capillary made of perfluoroalkoxy alkane (PFA) tubing (Index Health) with alternating coiled and straight segments of ID = 1.6 and 4.8 mm for flow pattern studies, and ID = 0.5, 1, and 1.6 mm and L = 17, 8.5, and 5 cm, respectively, for mass transfer rate studies. Deionized water (Milli-Q) was the aqueous solvent. MIBK 99% (Sigma-Aldrich) or 2-pentanol 99% (Sigma-Aldrich) was used as the organic solvent. Sodium fluorescein 99% (Sigma-Aldrich) and 9,10-diphenylanthracene 99% (Sigma-Aldrich) were used as the aqueous fluorescent dye and organic fluorescent, respectively, to contrast the two liquid phases during flow visualization.

The flow patterns were characterized using laser-induced fluorescence (LIF) of 250 μ M solution of sodium fluorescence in water and a 10 mM 9,10-diphenylanthracene solution in one of the selected organic solvents using a high-speed confocal microscope (Highspeed LSM 5 Live Duo) mounted with an inverter. Two laser sources with a wavelength of 488 and 405 nm were used for the fluorescence excitation of the aqueous and organic solvents, respectively. Images were captured using a Zeiss 1.25× and a 2.5× Plan-Neofluar objective lens at frame rates ranging from 30 to 108.1 fps. Further image analysis and processing of the flow patterns were conducted in ImageJ.

For mass transfer, an aqueous feed of 0.1 wt % HMF in water encounters a neat organic feed at the T-junction. As the biphasic mixture flows, the exit stream is collected in a 10 mL graduated cylinder placed directly below the outlet of the microchannel. As the two phases settle, immediate phase separation is observed for the solvent pairs. Using a 2 mL plastic pipet, the top organic phase is quickly removed from the graduated cylinder. Then small aliquots of the aqueous phase are pipetted into 300 μ L vials for postextraction analysis. The rate of mass transfer in the sampling zone is evaluated using the procedure reported in Zhao et al. 12

Computational Methods. CFD simulations of two-phase flow are conducted using the COMSOL Multiphysics 5.4 software. ⁵⁴ The laminar flow module is used to compute the velocity and pressure fields by solving the Navier–Stokes equation, eq 1.

Table 1. Features Define the Flow Patterns and Mass Transfer Rate in Liquid-Liquid Microchannels

features

aqueous phase (Aq)

organic phase (Org)

system-wide

aqueous phase (Aq)

interfacial tension (σ), total flow rate (Q), flow rate ratio (org/aq), total velocity of the system (U), where U interfacial tension (σ), total flow rate (U), and ength of the microchannel (U), where U interfacial tension (σ), total flow rate (U), and length of the microchannel (U), where U interfacial tension (σ), total flow rate (U), and length of the microchannel (U), where U is a features

kinematic viscosity (U), density (U), velocity (U), Capillary number (U), Reynolds number (U), Weber number (U), Ohnesorge number (U), and diffusivity (U)

$$\rho \frac{\mathrm{d}\mathbf{u}}{\mathrm{d}t} = -\nabla p + \nabla \cdot \tau + \rho \mathbf{g} \tag{1}$$

We use a two-phase flow, phase-field model, to define the parameters controlling the interface thickness and mobility. We specified the contact angle of the fluid to be 90°. The continuous species transfer (CST) model^{55,56} (eq 2) accounts for mass transfer between phases, for a given species *j*.

$$\frac{\partial C_j}{\partial t} + \nabla \cdot (C_j \cdot U) = \nabla \cdot (D_j \nabla C_j + \Phi_j)$$
(2)

This approach introduces a single-field representation and considers the concentration difference in the two phases at the interface with the discontinuity factor Φ , eq 3, where C is the single field concentration; D_j is the harmonic mean of the diffusivity of species j in the two phases weighed but the volume fractions, as in eq 4; α represents the aqueous volume fraction calculated using the phase field module; and K represents the partition coefficient, as in eq 5.

$$\Phi_{j} = -\left(\frac{D(1-K)}{\alpha + K(1-\alpha)}\right) \tag{3}$$

$$D_{j} = \frac{1}{\frac{\alpha}{D_{j,1}} + \frac{1 - \alpha}{D_{j,2}}} \tag{4}$$

$$K = \frac{C_{j,1}}{C_{j,2}} \tag{5}$$

The flow patterns and rate of mass transfer were independent of the cell number and size of discretization. Zero gradient for the pressure and no-slip boundary condition for the velocity are implemented at the wall. A fully developed flow is assumed at the inlet. At the outlet, the velocity is set to be zero-gradient and the pressure to be atmospheric. A simulation of a total of 1,000,000 to 2,000,000 nodes takes between 18 and 24 h computing time using 36 CPUs (Intel E5-2695 V4) on a high-performance computing cluster to obtain one flow pattern and 48–72 h for mass transfer data. For this work, we used water and ethyl acetate (EtAc), MIBK, or pentanol.

The volumetric mass transfer coefficient $(k_L a)$ is calculated using the outlet concentration of HMF in the organic phase using eq 6, derived from a simple biphasic plug flow mass transfer model. eq 6 is applied to CFD and experimental data. 21,28

$$k_{\rm L}a = {\rm rate~of~mass~transfer} = \frac{1}{\tau \left(\frac{K}{\varepsilon_{\rm aq}} + \frac{1}{\varepsilon_{\rm org}}\right)} {\rm ln} \left(\frac{C_{\rm org}^{\rm eq} - C_{\rm org}^{\rm in}}{C_{\rm org}^{\rm eq} - C_{\rm org}^{\rm out}}\right)$$
(6)

Here $k_{\rm L}$ is the mass transfer coefficient, and a is the specific interfacial area. τ represents the residence time, $\varepsilon_{\rm aq}$ and $\varepsilon_{\rm org}$ the volume fractions of the aqueous and organic phases, respectively, and $C_{\rm org}^{\rm eq}$, $C_{\rm org}^{\rm in}$, and $C_{\rm org}^{\rm out}$ the HMF concentration in the organic phase at equilibrium, inlet, and outlet of the microchannel, respectively.

Feature Importance. Principal component analysis (PCA) identifies the number of features required to capture the system's behavior. The properties and dimensionless groups of both phases, we find a total of 26 features (Table 1; definitions in SI). The material properties in the CFD model are listed in Table 1. The dimensionless groups are based on previous work. Apart from PCA, Feature importance can rank features for classifying flow patterns. A clustered covariance matrix can also be employed to group dependent variables. We implemented these algorithms using the sklearn library in Python. S8,59

Random Forest. We used a random forest model to predict flow patterns. This is an ensemble method based on the decision tree algorithm. Random forest is a commonly used supervised ML technique in data mining for predicting either the value (regression) or the class (classification) of target variables from input observations. The approach involves employing multiple decision trees, each splitting the data set into subsets by selecting variables that separate the observations at each tree node of the tree. Gini impurity (for variable selection) is combined with a randomized search method to set the hyperparameters (such as number of trees, max depth, min features, and bootstrapping) of the decision tree. The random forest algorithm is carried out using scikit-

The response space encompasses various flow patterns, while the predictors consist of the features. The experimental and CFD data are randomly split into a training set (80%) and a testing set (20%). A 3-fold cross-validation combined with a randomized search is employed to prevent overfitting. Because of the small data set generated in this work (~220 data obtained using CFD simulations and experiments), satisfactory accuracy was not achieved. Consequently, the random forest model was enhanced by leveraging a heterogeneous data set and active learning techniques, all while quantifying uncertainty (details provided below).

Active Learning. Creating a reliable surrogate model requires a sufficient data. Hence it is important to minimize the number of simulations and maximize the accuracy. We introduce the pool-based sampling method, which is a frequently used active learning algorithm, to select conditions for additional CFD simulations. ^{51,60}

A collection of data (unlabeled data set) was created by varying the diameter from 2 to 5 mm and the flow rate ratio from 1 to 4 while keeping Re < 2000. Multiple iterations were done to select points to maximize the accuracy of the random forest model. In each iteration, we used the random forest

model to predict flow patterns, and a data point was selected whose addition to the training data set (with the predicted label) would maximize accuracy (No. of correct predictions/ Size of the test data set). The selected data point was then simulated using CFD, and the corrected label was added to the training set (labeled data set). This process was repeated until the model accuracy did not improve. Using the pool-based method, 7 points were selected from the unlabeled pool, increasing the accuracy from 67 to 84%. Most points selected belong to the parallel, slug-drop, and irregular flow patterns, i.e., these were lacking types of data.

Hybrid (Heterogeneous) Data. We have enhanced our experimental and CFD data with mined flow pattern literature data that use T-junction liquid—liquid microchannels, laminar flow, and a consistent definition of flow patterns. This diversifies the solvents and diameters (from 0.2 to 5 mm), resulting in 730 total data points, as shown in Figure 2,4,13,19,26,28

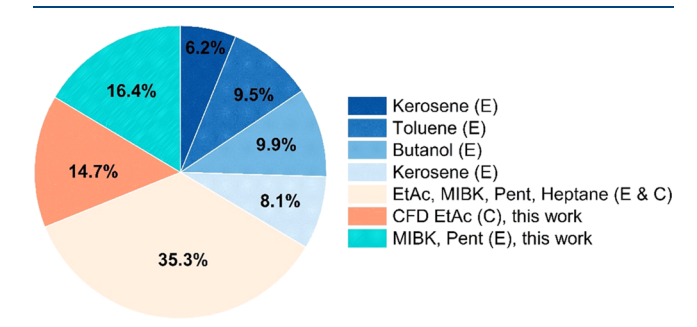


Figure 2. Distribution of flow pattern hybrid data set (E = experimental data, C = computational data, Pent. = Pentanol).

The experimental and CFD data are characterized by different degrees of uncertainty. Uncertainty in CFD stems from the solvers and meshing, resulting in 0.5% deviation (standard deviation of the outlet velocity simulated using d = 0.5 mm, q = 10 mL/min and a flow rate ratio = 1) in the predicted velocity, and the boundary condition regarding the wetting of the wall surface. Uncertainty in experiments is due to the high precision pumps. These pumps exhibit a 2%

deviation (value taken from the brochure of ReaXus LS Class High Performance Isocratic pumps).⁶¹ We use these uncertainties to quantify their impact on flow patterns (Scheme 1).^{52,62}

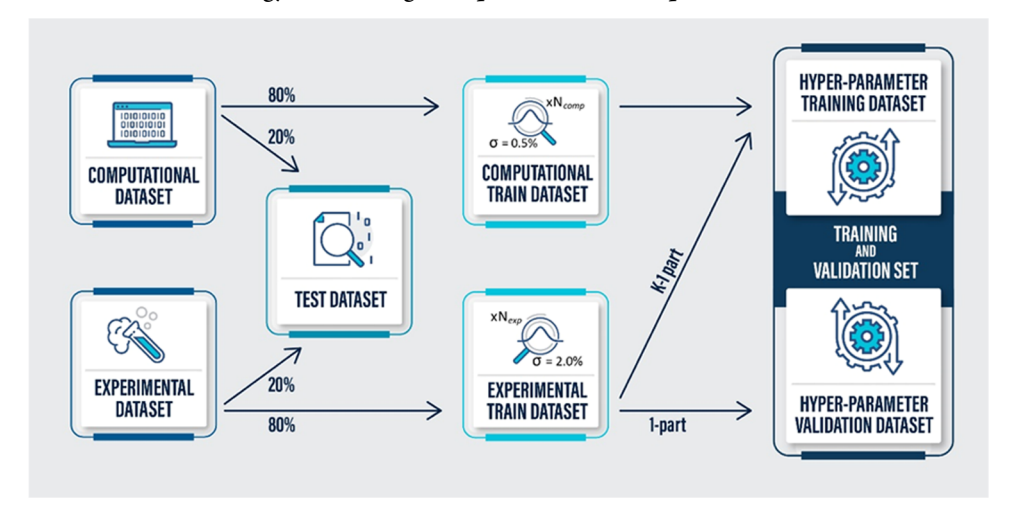
First, we divided the data into computational and experimental sets, splitting each into test and training sets (20:80 ratio). The test data of both are combined. We assume that uncertainties are normally distributed $(N(\mu,\sigma))$, where σ is 2 and 0.5% std. dev. for experimental and computational data, respectively. We sample $N_{\rm comp}$ and $N_{\rm exp}$ points for every computational and experimental data point, respectively, from the normal distribution with a velocity as the mean. In this work we assume $N_{\rm comp}=400$ and $N_{\rm exp}=100$. This approach weighs the data based on uncertainty $\left(\frac{\sigma_{\rm comp}}{\sigma_{\rm exp}} \propto \frac{N_{\rm exp}}{N_{\rm comp}}\right)$. The

convergence of the number of samples was also studied (refer to SI, Figure S2). As the velocity varies, we define the probability of observing a flow pattern.

We determine our random forest hyper-parameters using a modified 3-fold cross validation method combined with a randomized-grid search approach, ⁴⁶ where we train on 2 parts out of the 3 of the experimental and computational training data and minimize the error with respect to the remaining experimental training data.

Symbolic Genetic Regression. Conventionally, the mass transfer rate is represented with a power law model ($k_L a =$ $a^{\alpha}b^{\beta}c^{\delta}$; a, b, and c being features selected, such as Re, Ca, etc. and α , β , and δ being the respective exponents), and the parameters are estimated using logarithmic regression. Our analysis revealed that the power or the leading coefficient of the logarithmic model changes with solvent properties (refer to SI, Figure S3); i.e., the traditional model does not transfer from one solvent to another. Symbolic genetic regression⁶³ is a ML technique that "discovers" a mathematical expression to describe the data best. It first builds a population of naive random formulas to relate independent and dependent variables. Each successive generation is then evolved by selecting individuals from the population to undergo specified genetic operations based on the probabilities of the genetic operations as the input.

Scheme 1. Flowchart of the Methodology Combining Computational and Experimental Data



 $^{^{}a}N_{\text{comp}}, N_{\text{exp}}$ are the number of points sampled from the normal distribution of computational and experimental datasets; respectively.

We perform symbolic regression using the gplearn library of python, with an initial population size of 200,000 and a functional set including ('add (+)','sub (-)','div (/)', 'mul (*)', 'neg (-1*)', 'inv (1/)', "sqrt", "log", "exp"). The algorithm is run until the stopping criterion (mean square error <0.01) is reached or until 300 generations are created. The probabilities of various genetic operations were selected to maximize crossover and minimize point mutation.

The response space includes Da' (the ratio of Damkohler (I) to Damkohler (II); refer to SI for definitions). Da' includes τ multiplied by the mass transfer coefficient $(k_L a)$. The predictors are Ca, $\frac{Sc}{K}$, and $\frac{L}{d}$ selected using feature algorithms. The data collected using experiments are randomly split into training (80%) and testing (20%) sets.

RESULTS AND DISCUSSION

Liquid–Liquid Flow Patterns. Figure 3 shows the two-phase flow patterns (slug, drop, slug/droplet, and annular)

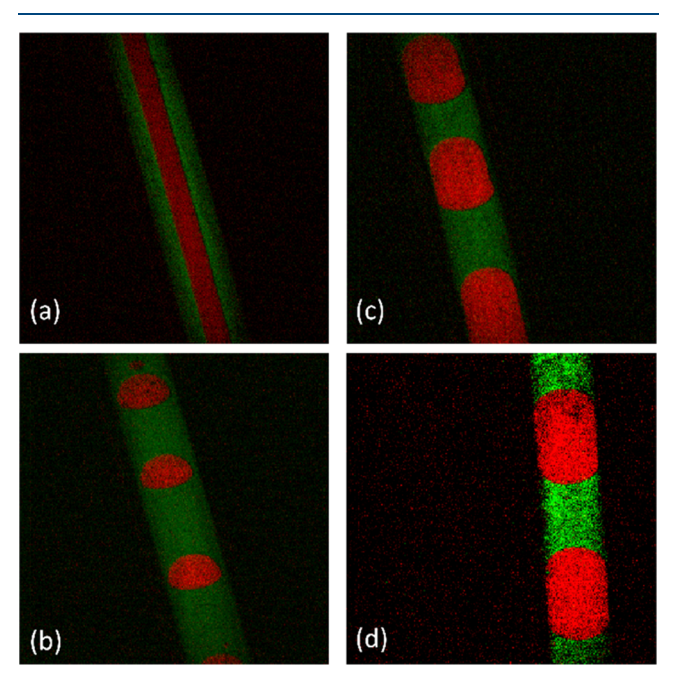


Figure 3. Experimental flow patterns: (a) Annular flow with q=10 mL/min, d=1.6 mm, org/aq = 3:1, 2-pentanol. (b) Slug/drop flow with q=8 mL/min, d=1.6 mm, org/aq = 3:1, 2-pentanol. (c) Drop flow with q=4 mL/min, d=1.6 mm, org/aq = 1:1, MIBK. (d) Slug flow with q=5 mL/min, d=1.6 mm, org/aq = 3:1, MIBK.

observed experimentally by using MIBK or 2-pentanol. We assessed the CFD model against new experiments for MIBK and 2-pentanol for d=1.6 mm and for EtAc using the experiments by Desir et al.⁴ for d=0.5 mm (at a flow rate ratio of 1). The flow patterns are in general agreement, as indicated by the confusion matrix in Figure S4. Figure 4 shows six computational flow patterns (slug, parallel, drop, slug/drop, annular, and irregular) using EtAc (EtAc was chosen as it shows all flow patterns within our range of velocity and diameter, and is another important solvent for HMF extraction). The organic phase is continuous (green in experiments and blue in computation), and the aqueous phase is the dispersed phase (red in experiments and computation).

Figure 5a,b,d, and 5c map the conditions for our experimental and computational flow patterns, respectively.

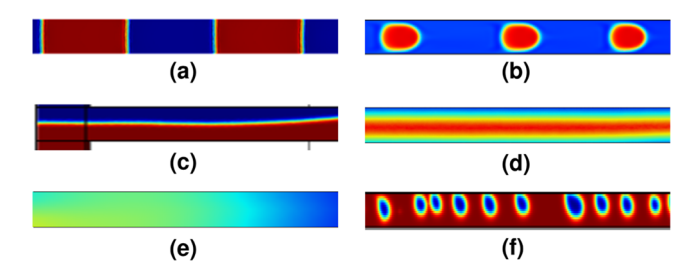


Figure 4. CFD flow patterns with EtAc: (a) slug flow for q = 0.2 mL/min, org/aq = 1:1, (b) droplet flow for q = 2 mL/min, org/aq = 1:1, (c) parallel flow for q = 5 mL/min, org/aq = 1:1, (d) annular flow for q = 7 mL/min, org/aq = 1:1, (e) irregular flow for q = 10 mL/min, d = 0.5 mm, org/aq = 1:1, and (f) slug-drop for q = 3 mL/min, org/aq = 4:1 (colors reversed). In all cases, d = 0.5 mm except for panel d where d = 2 mm.

As the diameter increases, different flow conditions (total volumetric flow rate, org/aq (v/v) ratio, various organic solvents) lead to varying patterns. Interestingly, slug flow still occurs using MIBK and 4.8 mm diameter because the velocity is lower for larger diameters and the same flow rate. For larger diameters, the parallel flow becomes prominent (Figure 5c). Solvents affect the flow patterns due to different interfacial tensions and viscosities, despite comparable densities (Table 2). At lower experimental flow rates (0.1-10 mL/min), no irregular flow is observed.^{4,6}

Feature Selection. Previous work for a constant diameter using PCA revealed that at least 6 features are needed to represent flow patterns.⁴ Figure 6 shows the mean decrease in impurity (average reduction in impurity when the feature is used as splitting criterion throughout the decision tree construction process) for various features. The Random Forest model was the best among models and was built using the top 6 features (further increase in number of features resulted in decreased accuracy and an increase in deviation for 3-fold cross validation). The selected features include the total velocity of the flow (U) and those of the organic (u_{org}) and the aqueous phase (u_{aq}) , the Capillary number of the aqueous phase (Ca_{aq}) , and the product of the Weber and the Ohnesorge numbers of the organic and aqueous phases (WeOhaq, WeOhorg). We find that We related dimensionless numbers are more important as we scaled up the microchannels.

Flow Pattern Prediction. Figure 7a shows the confusion matrix between the predicted and experimental flow patterns for the random forest model without uncertainty. The model with uncertainty is more predictive (Figure 7b) for annular, slug-drop, and irregular flow. The prediction probability (Figure S5) for the slug, slug-drop, and irregular flow is high. In contrast, parallel and annular flows are predicted less accurately due to multiple forces acting simultaneously without a single force being dominant in the transition from one force-dominated regime to another. Overall, both models are more than 85% accurate.

■ IMPACT OF DIAMETER ON THE SLUG FLOW

Slug flow is important due to the high degree of internal convection and large specific interfacial area that promote mass and heat transfer. 6,34,65 This pattern results from the interplay of interfacial, viscous, and inertial forces. The junction also breaks up the dispersed phase into slugs due to the pressure difference between phases. We have analyzed this flow pattern in more detail here. $^{27,66-68}$

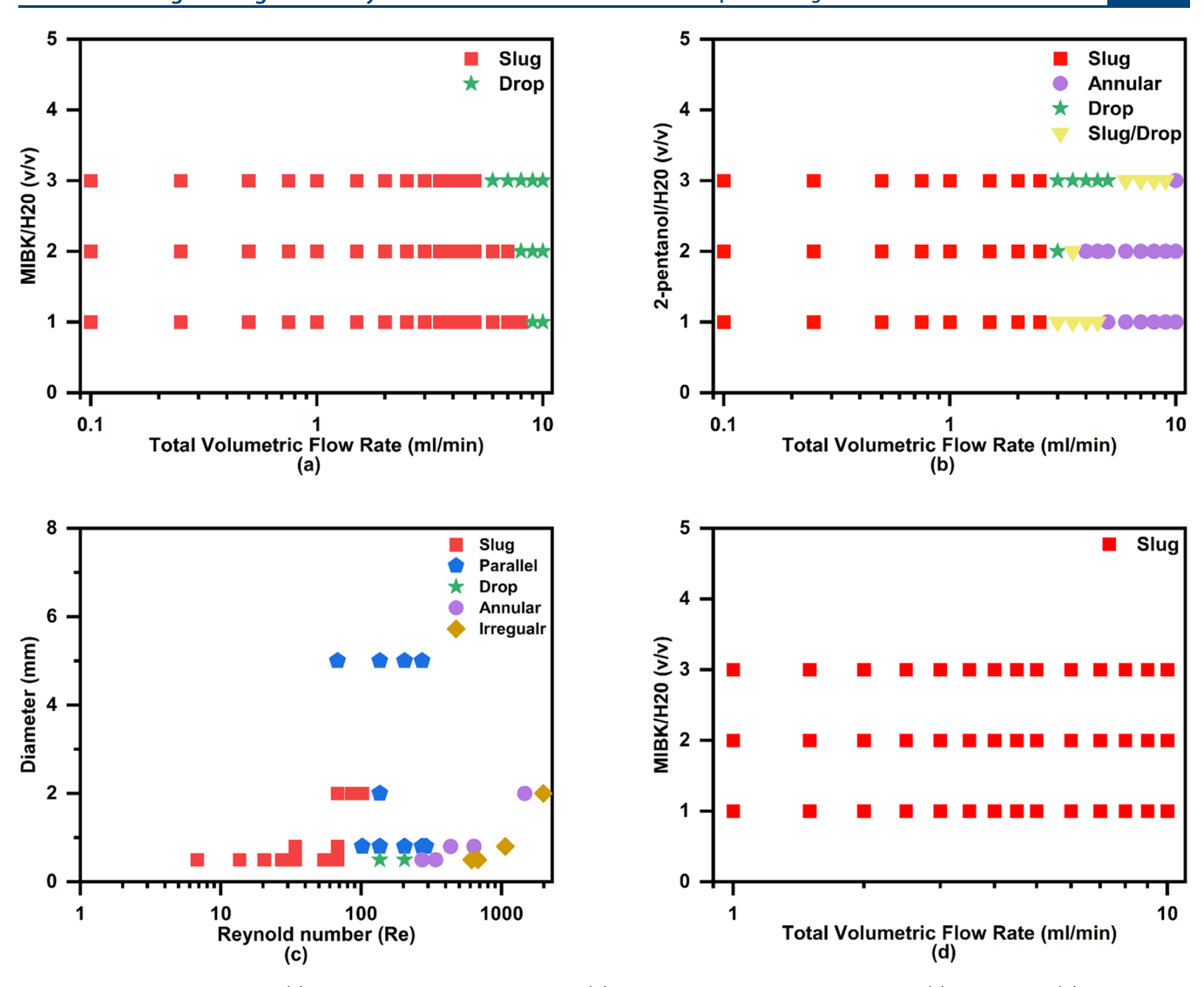


Figure 5. Maps of flow patterns: (a) Experiments, MIBK, d = 1.6 mm; (b) Experiments, 2-pentanol, d = 1.6 mm; (c) CFD, EtAc; (d) Experiments, MIBK, d = 4.8 mm.

Table 2. Organic Solvent Properties

organic solvent	dynamic viscosity (Pa.s)	density (kg m^{-3})	interfacial tension $(N\ m^{-1})$	diffusivity 6 (m 2 s $^{-1}$)	partition coefficient ⁶ (-)
EtAc	4.41×10^{-4}	900	0.0074	2.87×10^{-9}	1.4 ± 0.05
2-pentanol	3.47×10^{-3}	812	0.0034	3.81×10^{-10}	1.3 ± 0.07
MIBK	5.85×10^{-4}	684	0.0157	2.43×10^{-9}	1.1 ± 0.03

To capture the impact of diameter on the slug flow, we curate a data set derived from our experiments. We conducted simulations for 5 diameters and flow ratios from one to four. For a fixed diameter and a flow ratio, we increment the superficial velocity, keeping Re < 2100, to generate 400 points (a parametric continuation). The set of diameters, flow ratios, and velocities are then fed to the pretrained Random Forest model to predict the flow pattern. We define the maximum velocity for a given diameter and flow rate, for which we observe slug flow, as the critical point. These critical velocities are plotted in Figure 8 (marked points). The x-axis in Figure 8 shows the superficial velocity in the model, and the y-axis shows the flow rate ratio for this velocity. These results were verified using CFD calculations; slugs were seen at the maximum velocity graphed but not for a velocity 5% higher.

Figure 8 indicates slug flow even above 3 mm despite conventional belief. As the diameter or the flow rate ratio increases, the maximum velocity leading to slug flow decreases. The maximum velocity for slug flow above 4 mm is very low. CFD indicates that the slug flow at larger diameters (≥4 mm) happens because of the aqueous flow blocking the junction and then breaking into slugs. As the diameter increases, a trade-off between a higher throughput and slug flow benefits (higher mass and heat transfer rates) occurs. An interesting feature is symmetry breaking in the transition to no slugs. As the diameter increases, the Bo number increases, and hence, the impact of gravity on the slug over the interfacial force increases. The slug slowly starts deforming and gets attracted to the wall, breaking the symmetry. Results for different diameters for EtAc and water are listed in Figure 9. Figure 9c

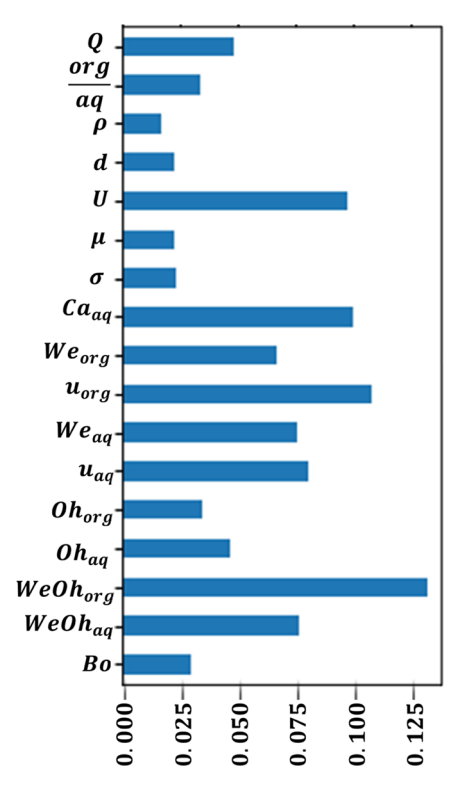
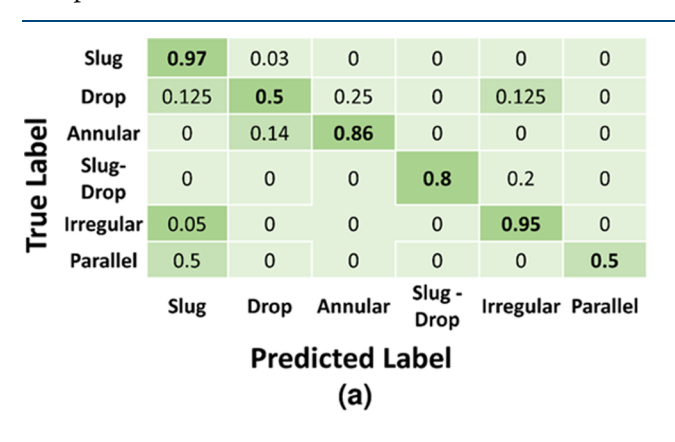


Figure 6. Feature importance for flow patterns (mean decrease in impurity: capacity of a feature to distinguish unique flow patterns for various features).

shows visible deformation in a 5 mm diameter microchannel, and Figure 9a depicts a symmetric slug for 0.5 mm diameter.

No significant symmetry changes were observed for drop and annular patterns with increasing diameters, but the parallel flow becomes prominent. A new flow pattern occurs in the transition from parallel flow to annular flow, which fluctuates between the parallel and annular flow with the organic phase touching the wall but after some time flowing in between the aqueous flow. This new flow pattern (Figure 9d) could be rationalized using gravitational and surface forces. The flow converts from parallel to annular flow due to surface forces making the aqueous phase leave the wall and flow in between the organic phase, but the aqueous flow gets attracted toward the other wall due to significant gravity and is converted into the parallel flow again as it flows along the wall. The irregular flow pattern vanishes above 2.4 mm.



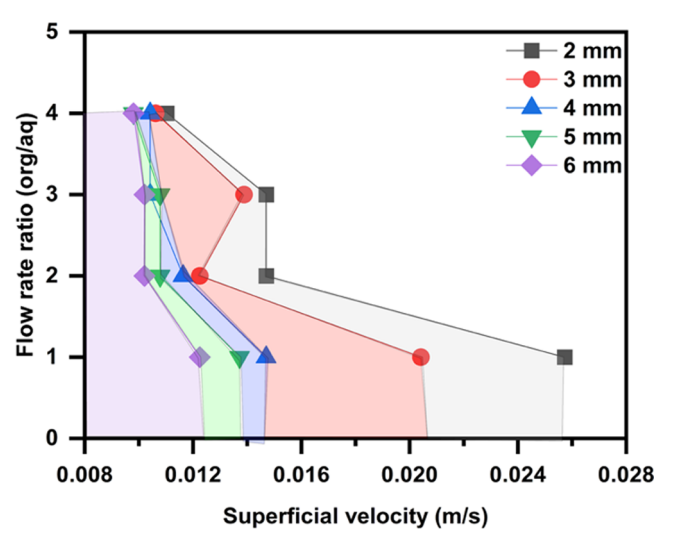


Figure 8. Critical total velocity leading to slug flow for different solvent ratios and diameters. The shaded region indicates the slug flow for each diameter; to the right of each line, no slug flow exists.

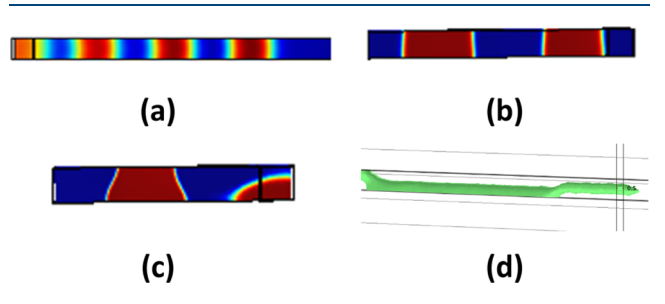


Figure 9. (a) Symmetric slugs with no deformation (d = 0.5 mm, and q = 0.7 mL/min). (b) Partially symmetric slugs with some deformation (d = 2 mm and q = 3 mL/min). (c) Deformed slugs with no symmetry (d = 5 mm and q = 40 mL/min). (d) New flow pattern.

MASS TRANSFER

Figure 10 shows the rate of mass transfer estimated experimentally for the three organic solvents at a fixed flow ratio of 1:1 as the total flow rate increases from 0.1 to 6 mL/min. The rate of mass transfer decreases with increasing diameter and increases with increasing velocity. We postulate that the mass transfer highly depends on the organic solvent properties, such as interfacial tension, viscosity, and density.

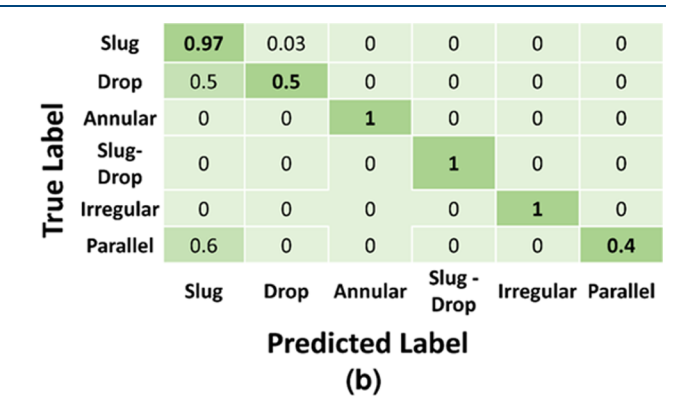


Figure 7. (a) Confusion matrix for the combined flow pattern test data set (20% hybrid flow pattern data set, ~146 data points). (b) Confusion matrix for the random forest model with uncertainty.

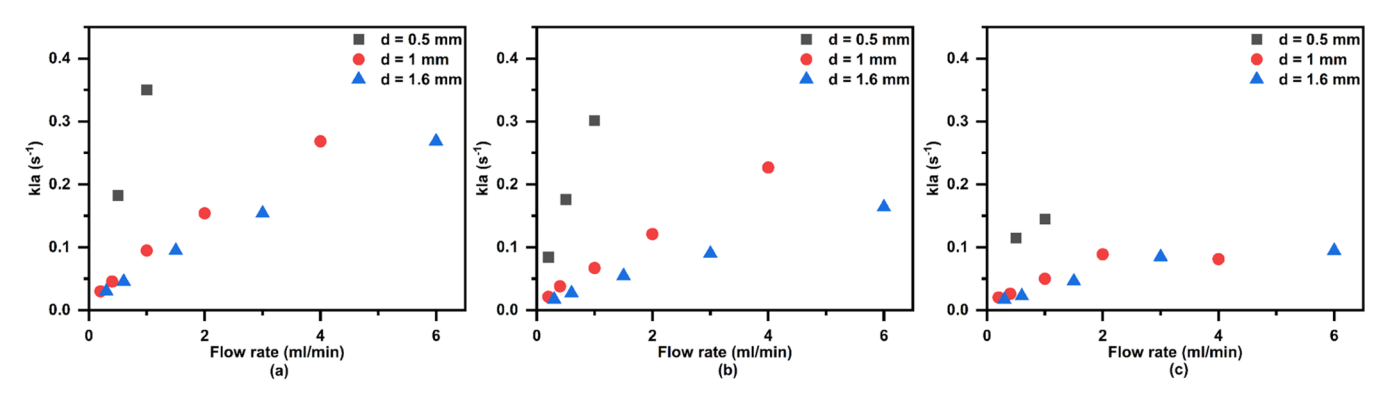


Figure 10. Experimentally estimated rate of mass transfer for (a) EtAc, (b) MIBK, and (c) pentanol.

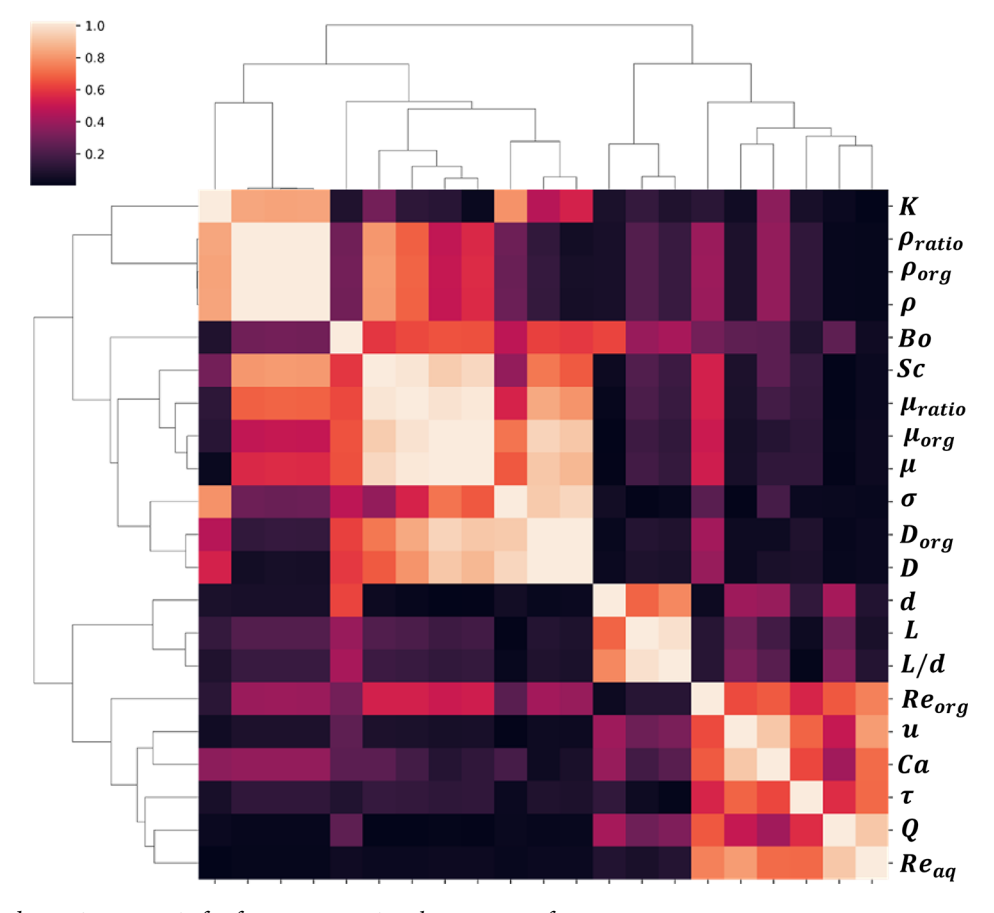


Figure 11. Clustered covariance matrix for features governing the mass transfer rate.

Experiments for EtAc, d=0.5 mm, L=17 cm, and Q ranging from 0.2 to 5 mL/min were simulated. Figure S6 shows the parity plot between the CFD-predicted and experimentally estimated rates of mass transfer. The maximum error is 5%. CFD was also used to study the concentration profile along the length (more information is provided in SI).

PCA suggests 4 features to represent the mass transfer rate (Figure S7). Figure 11 shows the clustered covariance matrix for the mass transfer rate features; 4 groups of interdependent features formed, and 1 feature from each group was chosen. The selected features include the residence time (τ) , Capillary number (Ca), Schmidt number over the partition coefficient ($\frac{Sc}{K}$, refer to SI for derivation), and the length over the diameter

 $\left(\frac{L}{d}\right)$. Ca and τ belong to the same covariance group but were chosen because Sc and K were combined into one feature.

Using symbolic genetic regression and the above groups, eq 7 was discovered to predict the rate of mass transfer. eq 7 relates the logarithm of Da' to the logarithm of Ca, $\frac{L}{d}$, and $\frac{Sc}{K}$ with α , β , γ , and δ as regression constants. $\frac{Sc}{K}$, $\frac{L}{d}$, and Ca capture the solvent properties, geometry of the system, and flow properties, respectively. eq 7 supports our hypothesis that the exponents in the power law model depend on solvent properties.

$$\log(Da') = \frac{\alpha \log\left(\frac{Sc}{K}\right) - \beta - \delta \log\left(\frac{L}{d}\right)}{\log(Ca) + \gamma}$$
(7)

The constants were calculated using the dual annealing minimization technique. ^{58,63,69} The normalized error between the actual and predicted rates of mass transfer was used as the cost function. The final form is eq 8. The parity plot between the predicted and experimental data is shown in Figure 12. The maximum deviation was 20%, and the average error was 13%.

$$\log(Da') = \frac{1.38 \log\left(\frac{Sc}{K}\right) - 0.972 - 0.84 \log\left(\frac{L}{d}\right)}{\log(Ca) + 0.525}$$
(8)

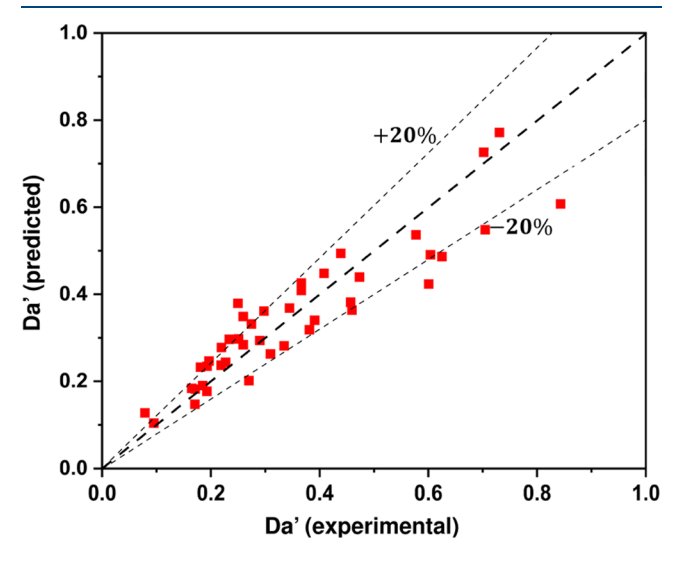


Figure 12. Parity of experimental and predicted Da'.

When $Ca \ll 1$, the denominator is negative. As the velocity increases, τ decreases, and Ca increases. However, τ affects $k_{\rm L}a$ more, and the rate of mass transfer increases. Similarly, as the length of the microchannel increases, the rate of mass transfer decreases due to significant increase in τ . With increasing diameter, the leading coefficient becomes negative, leading to decreasing mass transfer. The solvent properties (Table 2) are important: as the diffusivity, density, or partition coefficient increase, the rate of mass transport increases. The opposite happens with the viscosity.

The proposed model can be used to predict the rate of mass transfer and the concentration of the solute in the organic solvent, as shown in Figure S9. The predicted and CFD concentrations differ near the T junction, which enhances mixing. Upon formation of a stable flow pattern, the difference gradually decreases. Hence, the proposed model accurately predicts the concentration away from the junction.

Based on our previous work, scaling up from micro to milli scale is advantageous, as it decreases the capital cost and can increase the throughput. Figure S10 shows that organic solvents with lower Sc/K values (such as EtAc) exhibit higher mass transfer rates (predicted using eq 8) that can counterbalance the effect of increasing diameter, resulting in a slight reduction of mass transfer rate. Notably, as the diameter increases, the percentage decrease in the mass transfer rate due to the flow pattern change from slug to parallel diminishes. For example, Figure S11 indicates a ~50, 26.4, and 10% decrease when changing from slug to parallel flow for 0.5 1, and 1.6 mm, respectively, using an EtAc to aqueous ratio of 1:1 based on our CFD simulations. This decrease can be compensated by increasing the velocity and using alternative flow patterns, such

as the irregular flow pattern which shows higher mass transfer rate than the slug flow pattern. The predictive flow pattern and mass transfer models could guide design.

Uncertainty propagation \$\frac{52,62}{}\$ was used to estimate the accuracy of the proposed correlation. The HMF concentration in the organic phase shows an 4.8% standard deviation (s.d.), leading to a partition coefficient s.d. of 4%.⁷⁰ Uncertainty in the velocity results in uncertainty in the flow rate ratio (4% s.d, $u \sim N(\mu_u, 0.04) \rightarrow \frac{u_{\rm aq}}{u_{\rm org}} \sim N(\mu_{\rm ratio}, 0.04))$. As these are key variables in eq 6, propagation of uncertainty was done. Figure S12 shows the workflow to calculate the uncertainty in the rate of mass transfer. After introducing uncertainty in the velocity and partition coefficient, 2000 points were sampled from a normal distribution. This was repeated for the entire data set, and the parameters of the correlation were calculated in each iteration using the dual annealing method. These constants were inputted in a Gaussian inference algorithm and fitted with a normal distribution.⁵² The uncertainty in the rate of mass transfer was calculated to be \geq 50%.

As the data used to create the correlation were in the slug flow, we checked its applicability to other flow patterns. Mass transfer experiments in drop and parallel flow match well the model, as shown in Figure S13. Higher underprediction occurs for the drop flow probably due to the high specific area compared to the slug flow. The correlation could be further improved by increasing the size of the data set, including other flow patterns.

CONCLUSIONS

In this study, we examined flow patterns in liquid—liquid microchannels across various diameters and organic solvents by using both experimental methods and CFD simulations within a T-junction system. The flow pattern data were augmented using mined experimental data from the literature. The heterogeneous data were employed to create a random forest model of predicting flow patterns. Six (6) flow patterns were seen, namely, slug, parallel, drop, slug/drop, annular, and irregular.

The random forest model demonstrates accurate prediction capabilities for all flow patterns, except for regions near transition points. With an increase in diameter, gravitational forces influence the dispersed phase, leading to deformations along the slug flow interface. Parallel and droplet flows experience minimal gravity-induced impact, while new annular flow patterns emerge. Irregular flow patterns cease to occur above a 2.4 mm diameter at Re < 2000.

A mass transfer correlation was established by using experimental data and symbolic genetic regression. The rapid mixing at the junction promotes substantial transfer of HMF from the aqueous phase to the organic phase. This correlation effectively predicts mass transfer rates using dimensionless numbers such as Ca, Sc/K, and L/d. The correlation aligns with anticipated trends concerning the impact of velocity and diameter and also reveals, for the first time, the influence of solvent properties. The primary source of uncertainty in the mass transfer correlation lies in the correlation constants. The enhancement of the correlation could be achieved through the inclusion of additional data spanning other flow patterns.

ASSOCIATED CONTENT

Supporting Information

The Supporting Information is available free of charge at https://pubs.acs.org/doi/10.1021/acs.iecr.3c02284.

Definitions, Parity plots, CFD experimental conditions and data, and computational data analysis (PDF)

AUTHOR INFORMATION

Corresponding Authors

Marianthi Ierapetritou — Department of Chemical and Biomolecular Engineering, University of Delaware, Newark, Delaware 19716, United States; Catalysis Center for Energy Innovation and Delaware Energy Institute, University of Delaware, Newark, Delaware 19716, United States;

orcid.org/0000-0002-1758-9777; Email: mgi@udel.edu

Dionisios G. Vlachos — Department of Chemical and Biomolecular Engineering, University of Delaware, Newark, Delaware 19716, United States; Catalysis Center for Energy Innovation and Delaware Energy Institute, University of Delaware, Newark, Delaware 19716, United States; orcid.org/0000-0002-6795-8403; Email: vlachos@udel.edu

Authors

Arnav Mittal — Department of Chemical and Biomolecular Engineering, University of Delaware, Newark, Delaware 19716, United States

Souryadeep Bhattacharyya — Department of Chemical and Biomolecular Engineering, University of Delaware, Newark, Delaware 19716, United States

Matthew Marino – Department of Chemical and Biomolecular Engineering, University of Delaware, Newark, Delaware 19716, United States

Tai-Ying Chen – Department of Chemical and Biomolecular Engineering, University of Delaware, Newark, Delaware 19716, United States

Pierre Desir – Department of Chemical and Biomolecular Engineering, University of Delaware, Newark, Delaware 19716, United States

Complete contact information is available at: https://pubs.acs.org/10.1021/acs.iecr.3c02284

Notes

The authors declare no competing financial interest.

ACKNOWLEDGMENTS

T.-Y.C., P.D., M.M., and S.B. were supported by the RAPID manufacturing institute, through the Department of Energy (DOE) Advanced Manufacturing Office (AMO), award number DE-EE0007888-7.6. RAPID projects at the University of Delaware were also made possible in part by funding provided by the State of Delaware. A.M. was primarily supported by the National Science Foundation under Grant No. 2134471. D.G.V. dedicates this article to Dmitry Murzin, his long-lasting friend.

REFERENCES

- (1) Jensen, K. F. Microreaction engineering is small better? *Chem. Eng. Sci.* **2001**, *56* (2), 293–303.
- (2) Hartman, R. L.; Jensen, K. F. Microchemical systems for continuous-flow synthesis. *Lab Chip* **2009**, *9* (17), 2495.

- (3) Jähnisch, K.; Hessel, V.; Löwe, H.; Baerns, M. Chemistry in Microstructured Reactors. *Angew. Chem., Int. Ed.* **2004**, 43 (4), 406–446
- (4) Desir, P.; Chen, T.-Y.; Bracconi, M.; Saha, B.; Maestri, M.; Vlachos, D. G. Experiments and computations of microfluidic liquid—liquid flow patterns. *React. Chem. Eng.* **2020**, 5 (1), 39–50.
- (5) Desir, P.; Vlachos, D. G. Intensified reactive extraction for the acid-catalyzed conversion of fructose to 5-hydroxymethyl furfural. *Chem. Eng. J.* **2022**, 428, No. 132556.
- (6) Chen, T.-Y.; Desir, P.; Bracconi, M.; Saha, B.; Maestri, M.; Vlachos, D. G. Liquid-Liquid Microfluidic Flows for Ultrafast 5-Hydroxymethyl Furfural Extraction. *Ind. Eng. Chem. Res.* **2021**, *60* (9), 3723–3735.
- (7) Desir, P.; Saha, B.; Vlachos, D. G. Ultrafast flow chemistry for the acid-catalyzed conversion of fructose. *Energy Environ. Sci.* **2019**, *12* (8), 2463–2475.
- (8) Gervais, T.; Jensen, K. F. Mass transport and surface reactions in microfluidic systems. *Chem. Eng. Sci.* **2006**, *61* (4), 1102–1121.
- (9) Günther, A.; Khan, S. A.; Thalmann, M.; Trachsel, F.; Jensen, K. F. Transport and reaction in microscale segmented gas—liquid flow. *Lab Chip* **2004**, *4* (4), 278–286.
- (10) Yue, J.; Chen, G.; Yuan, Q.; Luo, L.; Gonthier, Y. Hydrodynamics and mass transfer characteristics in gas—liquid flow through a rectangular microchannel. *Chem. Eng. Sci.* **2007**, *62* (7), 2096–2108.
- (11) Jaiswal, P.; Kumar, Y.; Shukla, R.; Nigam, K. D. P.; Panda, D.; Guha Biswas, K. Covalently Immobilized Nickel Nanoparticles Reinforce Augmentation of Mass Transfer in Millichannels for Two-Phase Flow Systems. *Ind. Eng. Chem. Res.* **2022**, *61* (10), 3672–3684.
- (12) Zhao, Y.; Chen, G.; Yuan, Q. Liquid-liquid two-phase mass transfer in the T-junction microchannels. *AIChE J.* **2007**, 53 (12), 3042–3053.
- (13) Zhao, Y.; Chen, G.; Yuan, Q. Liquid-liquid two-phase flow patterns in a rectangular microchannel. *AIChE J.* **2006**, *52* (12), 4052–4060.
- (14) Bothe, D.; Stemich, C.; Warnecke, H.-J. Mixing in a T-shaped microreactor: scales and quality of mixing. In *Computer Aided Chemical Engineering*; Elsevier, 2006; Vol. 21, pp 351–357.
- (15) Nagy, K. D.; Shen, B.; Jamison, T. F.; Jensen, K. F. Mixing and Dispersion in Small-Scale Flow Systems. *Org. Process Res. Dev.* **2012**, 16 (5), 976–981.
- (16) Ahmed-Omer, B.; Brandt, J. C.; Wirth, T. Advanced organic synthesis using microreactor technology. *Org. Biomol. Chem.* **2007**, 5 (5), 733–740.
- (17) Halder, R.; Lawal, A.; Damavarapu, R. Nitration of toluene in a microreactor. *Catal. Today* **2007**, *125* (1–2), 74–80.
- (18) Qiu, L.; Wang, K.; Zhu, S.; Lu, Y.; Luo, G. Kinetics study of acrylic acid polymerization with a microreactor platform. *Chem. Eng. J.* **2016**, 284, 233–239.
- (19) Wang, X.; Wang, Y.; Li, F.; Li, L.; Ge, X.; Zhang, S.; Qiu, T. Scale-up of microreactor: Effects of hydrodynamic diameter on liquid—liquid flow and mass transfer. *Chem. Eng. Sci.* **2020**, 226, No. 115838.
- (20) Rossetti, I.; Compagnoni, M. Chemical reaction engineering, process design and scale-up issues at the frontier of synthesis: Flow chemistry. *Chem. Eng. J.* **2016**, *296*, 56–70.
- (21) Kashid, M. N.; Renken, A.; Kiwi-Minsker, L. Gas-liquid and liquid-liquid mass transfer in microstructured reactors. *Chem. Eng. Sci.* **2011**, *66* (17), 3876–3897.
- (22) Zha, L.; Pu, X.; Shang, M.; Li, G.; Xu, W.; Lu, Q.; Su, Y. A study on the micromixing performance in microreactors for polymer solutions. *AIChE J.* **2018**, *64* (9), 3479–3490.
- (23) Dessimoz, A.-L.; Cavin, L.; Renken, A.; Kiwi-Minsker, L. Liquid—liquid two-phase flow patterns and mass transfer characteristics in rectangular glass microreactors. *Chem. Eng. Sci.* **2008**, *63* (16), 4035–4044.
- (24) Wang, S.; Zhang, Z.; Liu, B. Catalytic Conversion of Fructose and 5-Hydroxymethylfurfural into 2,5-Furandicarboxylic Acid over a

- Recyclable Fe₃O₄-CoO_x Magnetite Nanocatalyst. *ACS Sustainable Chem. Eng.* **2015**, 3 (3), 406-412.
- (25) Jaiswal, P.; Kumar, Y.; Panda, D.; Guha Biswas, K. Vibration in Microchannel Causes Greater Enhancement of Mass Transfer in Toluene–Acetic Acid–Water System. *Ind. Eng. Chem. Res.* **2021**, *60* (50), 18464–18476.
- (26) Yagodnitsyna, A. A.; Kovalev, A. V.; Bilsky, A. V. Flow patterns of immiscible liquid-liquid flow in a rectangular microchannel with T-junction. *Chem. Eng. J.* **2016**, *303*, 547–554.
- (27) Kashid, M. N.; Agar, D. W. Hydrodynamics of liquid—liquid slug flow capillary microreactor: Flow regimes, slug size and pressure drop. *Chem. Eng. J.* **2007**, *131* (1–3), 1–13.
- (28) N Kashid, M.; Renken, A.; Kiwi-Minsker, L. Influence of Flow Regime on Mass Transfer in Different Types of Microchannels. *Ind. Eng. Chem. Res.* **2011**, *50* (11), 6906–6914.
- (29) Gobby, D.; Angeli, P.; Gavriilidis, A. Mixing characteristics of T-type microfluidic mixers. *J. Micromech. Microeng.* **2001**, *11* (2), 126–132.
- (30) Hessel, V.; Kralisch, D.; Kockmann, N.; Noël, T.; Wang, Q. Novel Process Windows for Enabling, Accelerating, and Uplifting Flow Chemistry. *ChemSusChem* **2013**, *6* (5), 746–789.
- (31) Zhang, J.; Ling, S. D.; Chen, A.; Chen, Z.; Ma, W.; Xu, J. The liquid—liquid flow dynamics and droplet formation in a modified step T-junction microchannel. *AIChE J.* **2022**, *68* (6), No. e17611, DOI: 10.1002/aic.17611.
- (32) Chaoqun, Y.; Yuchao, Z.; Chunbo, Y.; Minhui, D.; Zhengya, D.; Guangwen, C. Characteristics of slug flow with inertial effects in a rectangular microchannel. *Chem. Eng. Sci.* **2013**, *95*, 246–256.
- (33) Kashid, M. N.; Gerlach, I.; Goetz, S.; Franzke, J.; Acker, J. F.; Platte, F.; Agar, D. W.; Turek, S. Internal Circulation within the Liquid Slugs of a Liquid–Liquid Slug-Flow Capillary Microreactor. *Ind. Eng. Chem. Res.* **2005**, *44* (14), 5003–5010.
- (34) Zhao, C. X.; Middelberg, A. P. J. Two-phase microfluidic flows. *Chem. Eng. Sci.* **2011**, *66* (7), 1394–1411.
- (35) Burns, M. A.; Johnson, B. N.; Brahmasandra, S. N.; Handique, K.; Webster, J. R.; Krishnan, M.; Sammarco, T. S.; Man, P. M.; Jones, D.; Heldsinger, D.; et al. An Integrated Nanoliter DNA Analysis Device. *Science* **1998**, 282 (5388), 484–487.
- (36) Surmeian, M.; Hibara, A.; Slyadnev, M.; Uchiyama, K.; Hisamoto, H.; Kitamori, T. DISTRIBUTION OF METHYL RED ON THE WATER-ORGANIC LIQUID INTERFACE IN A MICROCHANNEL. *Anal. Lett.* **2001**, 34 (9), 1421–1429.
- (37) Hisamoto, H.; Horiuchi, T.; Tokeshi, M.; Hibara, A.; Kitamori, T. On-Chip Integration of Neutral Ionophore-Based Ion Pair Extraction Reaction. *Anal. Chem.* **2001**, *73* (6), 1382–1386.
- (38) Assmann, N.; Ładosz, A.; Rudolf Von Rohr, P. Continuous Micro Liquid-Liquid Extraction. *Chem. Eng. Technol.* **2013**, 36 (6), 921–936.
- (39) Wang, K.; Luo, G. Microflow extraction: A review of recent development. *Chem. Eng. Sci.* **2017**, *169*, 18–33.
- (40) Marre, S.; Jensen, K. F. Synthesis of micro and nanostructures in microfluidic systems. *Chem. Soc. Rev.* **2010**, 39 (3), 1183.
- (41) Chheda, J. N.; Román-Leshkov, Y.; Dumesic, J. A. Production of 5-hydroxymethylfurfural and furfural by dehydration of biomass-derived mono- and poly-saccharides. *Green Chem.* **2007**, *9* (4), 342–350.
- (42) Salak Asghari, F.; Yoshida, H. Acid-Catalyzed Production of 5-Hydroxymethyl Furfural from Fructose in Subcritical Water. *Ind. Eng. Chem. Res.* **2006**, 45 (7), 2163–2173.
- (43) Plouffe, P.; Bittel, M.; Sieber, J.; Roberge, D. M.; Macchi, A. On the scale-up of micro-reactors for liquid—liquid reactions. *Chem. Eng. Sci.* **2016**, *143*, 216–225.
- (44) Tsaoulidis, D.; Angeli, P. Effect of channel size on mass transfer during liquid—liquid plug flow in small scale extractors. *Chem. Eng. J.* **2015**, 262, 785–793.
- (45) Kashid, M. N.; Gupta, A.; Renken, A.; Kiwi-Minsker, L. Numbering-up and mass transfer studies of liquid—liquid two-phase microstructured reactors. *Chem. Eng. J.* **2010**, *158* (2), 233–240.

- (46) Qian, J.-y.; Li, X.-j.; Wu, Z.; Jin, Z.-j.; Sunden, B. A comprehensive review on liquid—liquid two-phase flow in microchannel: flow pattern and mass transfer. *Microfluid. Nanofluid.* **2019**, 23 (10), 116.
- (47) Sattari-Najafabadi, M.; Nasr Esfahany, M.; Wu, Z.; Sundén, B. The effect of the size of square microchannels on hydrodynamics and mass transfer during liquid-liquid slug flow. *AIChE J.* **2017**, *63* (11), 5019–5028.
- (48) Li, G.; Shang, M.; Song, Y.; Su, Y. Characterization of liquid-liquid mass transfer performance in a capillary microreactor system. *AIChE J.* **2018**, *64* (3), 1106–1116.
- (49) Kashid, M. N.; Agar, D. W.; Turek, S. CFD modelling of mass transfer with and without chemical reaction in the liquid—liquid slug flow microreactor. *Chem. Eng. Sci.* **2007**, *62* (18–20), 5102–5109.
- (50) Zhang, J.; Zhou, Y.; Chen, Z.; Xu, J. Hydrodynamics and liquid—liquid mass transfer in gas—liquid—liquid three-phase flow in a cross microchannel. *Chem. Eng. Sci.* **2023**, 273, No. 118657.
- (51) Settles, B. Active Learning; Morgan & Claypool: San Rafael, Calif., 2012.
- (52) Chen, W.; Cohen, M.; Yu, K.; Wang, H.-L.; Zheng, W.; Vlachos, D. G. Experimental data-driven reaction network identification and uncertainty quantification of CO2-assisted ethane dehydrogenation over Ga2O3/Al2O3. *Chem. Eng. Sci.* **2021**, 237, No. 116534.
- (53) Chen, T.-Y.; Hsiao, Y. W.; Baker-Fales, M.; Cameli, F.; Dimitrakellis, P.; Vlachos, D. G. Microflow chemistry and its electrification for sustainable chemical manufacturing. *Chem. Sci.* **2022**, *13* (36), 10644–10685.
- (54) COMSOL Multiphysics v. 5.4. www.comsol.com. COMSOL AB, Stockholm, Sweden.
- (55) Hirt, C. W.; Nichols, B. D. Volume of fluid (VOF) method for the dynamics of free boundaries. *J. Comput. Phys.* **1981**, 39 (1), 201–225.
- (56) Haroun, Y.; Legendre, D.; Raynal, L. Volume of fluid method for interfacial reactive mass transfer: Application to stable liquid film. *Chem. Eng. Sci.* **2010**, *65* (10), 2896–2909.
- (57) López-Guajardo, E. A.; Delgado-Licona, F.; Álvarez, A. J.; Nigam, K. D. P.; Montesinos-Castellanos, A.; Morales-Menendez, R. Process intensification 4.0: A new approach for attaining new, sustainable and circular processes enabled by machine learning. *Chem. Eng. Process.* **2022**, *180*, No. 108671.
- (58) Hastie, T.; Tibshirani, R.; Friedman, J. H. *The Elements of Statistical Learning: Data Mining, Inference, and Prediction*, 2nd ed.; Springer Series in Statistics: New York, NY, 2009.
- (59) Pedregosa, F.; Varoquaux, G.; Gramfort, A.; Michel, V.; Thirion, B.; Grisel, O.; Blondel, M.; Prettenhofer, P.; Weiss, R.; Dubourg, V.; et al. Scikit-learn: Machine Learning in Python. *J. Mach. Learn. Res.* **2011**, *12* (85), 2825–2830.
- (60) Wang, Y.; Chen, T.-Y.; Vlachos, D. G. NEXTorch: A Design and Bayesian Optimization Toolkit for Chemical Sciences and Engineering. J. Chem. Inf. Model. 2021, 61 (11), 5312–5319.
- (61) Reaxus LS Class. https://www.teledyneisco.com/en-us/Pumps_/Pumps%20Documents/Datasheets/ReaXus%20LS%20Class%20Datasheet.pdf (accessed July 08, 2023).
- (62) Feng, J.; Lansford, J. L.; Katsoulakis, M. A.; Vlachos, D. G. Explainable and trustworthy artificial intelligence for correctable modeling in chemical sciences. *Sci. Adv.* **2020**, *6* (42), No. eabc3204.
- (63) Ansari, M.; Gandhi, H. A.; Foster, D. G.; White, A. D. Iterative symbolic regression for learning transport equations. *AIChE* **2022**, *68* (6), No. e17695, DOI: 10.1002/aic.17695.
- (64) Chen, W.; Malhotra, A.; Yu, K.; Zheng, W.; Plaza-Gonzalez, P. J.; Catala-Civera, J. M.; Santamaria, J.; Vlachos, D. G. Intensified microwave-assisted heterogeneous catalytic reactors for sustainable chemical manufacturing. *Chem. Eng. J.* **2021**, *420*, No. 130476.
- (65) Chen, T.-Y.; Cheng, Z.; Desir, P.; Saha, B.; Vlachos, D. G. Fast microflow kinetics and acid catalyst deactivation in glucose conversion to 5-hydroxymethylfurfural. *React. Chem. Eng.* **2021**, *6* (1), 152–164.

- (66) Shui, L.; van den Berg, A.; Eijkel, J. C. T. Capillary instability, squeezing, and shearing in head-on microfluidic devices. *J. Appl. Phys.* **2009**, *106* (12), No. 124305.
- (67) Yang, L.; Nieves-Remacha, M. J.; Jensen, K. F. Simulations and analysis of multiphase transport and reaction in segmented flow microreactors. *Chem. Eng. Sci.* **2017**, *169*, 106–116.
- (68) Yang, Z.; Qi, W.; Su, R.; He, Z. Selective Synthesis of 2,5-Diformylfuran and 2,5-Furandicarboxylic Acid from 5-Hydroxymethylfurfural and Fructose Catalyzed by Magnetically Separable Catalysts. *Energy Fuels* **2017**, *31* (1), 533–541.
- (69) Ben Chaabene, W.; Nehdi, M. L. Genetic programming based symbolic regression for shear capacity prediction of SFRC beams. *Constr. Build. Mater.* **2021**, 280, No. 122523.
- (70) Li, G.; Pu, X.; Shang, M.; Zha, L.; Su, Y. Intensification of liquid-liquid two-phase mass transfer in a capillary microreactor system. *AIChE J.* **2019**, *65* (1), 334–346.